Publications of the Astronomical Society of Australia (2025), **42**, e135, 15 pages
doi:10.1017/pasa.2025.10100

CAMBRIDGE
UNIVERSITY PRESS

Research Article

Determining ideal fields for Epoch of Reionisation science using the 21 cm line

Eric Jong[1,2], Cathryn Trott[1,2], Chuneeta D. Nunhokee[1,2] and Qian Zheng[3]

[1]International Centre for Radio Astronomy Research, Curtin University, Bentley, WA, Australia, [2]ARC Centre of Excellence for All-Sky Astrophysics in 3D (ASTRO 3D), Bentley, Australia and [3]Shanghai Astronomical Observatory, Chinese Academy of Sciences, Shanghai, P. R. China

Abstract

The upcoming Square Kilometre Array Low Frequency (SKA-Low) interferometer will have the required sensitivity to detect the 21 cm line from neutral hydrogen during the Epoch of Reionisation (EoR). In preparation, we investigated the suitability of different fields for EoR science with the 21 cm line, using existing observations of candidate fields from the Murchison Widefield Array (MWA). Various image and calibration metrics were extracted from archival MWA observations centred on $z \sim 6.8$. We explore the usefulness of these metrics and compare their behaviour between different fields of interest. In addition, a theoretical approach to quantifying the impact of different fields on the power spectrum is also provided. Gain uncertainties were calculated based on the positions of the calibrators within the beam. These uncertainties were then propagated into visibilities to produce cylindrical power spectra for various fields. Using these metrics in combination with the power spectra, we confirm that EoR0 (R.A. = 0 deg, Dec = −27.0 deg) is an ideal EoR field and discuss the interesting behaviour of other fields.

Keywords: (cosmology:) dark ages; reionization; first stars; instrumentation: interferometers; (cosmology:) early Universe; cosmology: observations

(Received 6 June 2025; revised 17 September 2025; accepted 18 September 2025)

1. Introduction

From the Cosmic Dawn (CD, $z \sim 30 - 10$) through the Epoch of Reionisation (EoR, $z \sim 10 - 5.3$), the Universe underwent incredible change. During the CD, neutral hydrogen (HI) atoms that formed at Recombination start to collapse gravitationally and form the first luminous objects. These objects then re-ionised the HI that surrounded them and created 'bubbles' of ionised hydrogen (HII) – the beginning of EoR.

Over time, with the formation of new luminous sources and bubbles continuously expanding, we arrive at the bright and mostly ionised Universe of the present day. Understanding the evolution of hydrogen helps to reveal the properties of the first stars, such as the processes involved in the formation of these stars, their mass, when they first formed, and how the Universe evolved from a smooth matter distribution to its complex structures of today (Furlanetto, Peng Oh, & Briggs 2006; Zheng et al. 2020; Koopmans et al. 2015). Evidently, there lies a wealth of knowledge crucial to our understanding of the Universe.

To trace neutral hydrogen, the 21 cm wavelength photon produced by the hyperfine transition in the ground state of hydrogen is of interest. This particular wavelength is not easily re-absorbed by other hydrogen atoms; hence, it travels through the neutral hydrogen medium unimpeded. Although it may take multiple millions of years for a single hydrogen atom to produce this signal (Storey et al. 1994), the abundance of hydrogen ensures that we can probe these time periods. For a thorough review of the history of HI in the Universe, see Pritchard & Loeb (2012), Koopmans et al. (2015), Furlanetto, Peng Oh, & Briggs (2006), and references therein.

Major efforts in EoR science lie in measuring the brightness temperature of the 21 cm line at some particular redshift, through a variety of statistics; the brightness temperature spatial power spectrum is commonly used. This is undertaken through observations with radio interferometers such as the Murchison Widefield Array (MWA, Tingay et al. 2013; Wayth et al. 2018), LOw-Frequency Array (LOFAR, Haarlem et al. 2013), New Extension in Nançay Upgrading LOFAR (NENUFAR, Zarka et al. 2015), Hydrogen Epoch of Reionization Array (HERA, DeBoer et al. 2017), the Giant Metre-wave Radio Telescope (GMRT, Swarup et al. 1991), and the Long Wavelength Array (LWA, Ellingson et al. 2009). Results for the upper limit on the 21 cm brightness temperature have also been reported by these instruments: MWA (Trott et al. 2020; Nunhokee et al. 2025), LOFAR (Mertens et al. 2020; Acharya et al. 2024; Mertens et al. 2025), NenuFAR (Munshi et al. 2024; Munshi et al. 2025), HERA (Abdurashidova et al. 2022; HERA Collaboration et al. 2023), GMRT (Paciga et al. 2011), and LWA (Eastwood et al. 2019).

There are many challenges in the measurement of the 21 cm signal. Radio signals from astrophysical and human sources produce foreground contamination; processes such as synchrotron emission, free-free scattering, bright radio sources, radio emission from digital television channels, FM radio emissions, and satellites are orders of magnitude brighter than the 21 cm line (Bowman & Rogers 2010; Chapman & Jelic 2019; Offringa et al. 2015). Imprecise calibration solutions have also been a challenge

Corresponding author: Eric Jong; Email: eric.jong@postgrad.curtin.edu.au.

Cite this article: Jong E, Trott C, Nunhokee CD and Zheng Q. (2025) Determining ideal fields for Epoch of Reionisation science using the 21 cm line. *Publications of the Astronomical Society of Australia* **42**, e135, 1–15. https://doi.org/10.1017/pasa.2025.10100

in these experiments. Spectral features in the calibration solutions can propagate into the power spectra and affect our ability to make a measurement. Spectral features caused by using an incomplete sky model in the calibration step (Barry et al. 2016; Ewall-Wice et al. 2017; Procopio et al. 2017) or errors in beam responses (Nunhokee et al. 2020; Chokshi et al. 2024; Brackenhoff et al. 2025) have been shown to overwhelm the feeble 21 cm signal. Clearly, the study of these processes is crucial to minimising their effect and for the success of EoR science.

This paper aims to investigate one such challenge, that is, how different parts of the sky impact data calibration and in turn determine the ideal fields of the sky for EoR observations with Square Kilometre Array Low Frequency (SKA-Low). The calibration is sensitive to different parts of the sky due to the density of sources, brightness distribution of sources, and the types of sources present (compact or extended).

The MWA collaboration has selected two regions of the sky which are deemed fit for EoR science: EoR0 (R.A. $= 0°$, Dec $= -27°$) and EoR1(R.A. $= 60°$, Dec $= -27°$). EoR0 is described as containing a few, bright resolved sources allowing for 'easier' calibration (Jacobs et al. 2016). EoR1 was chosen for similar reasons, containing another cold patch of the sky.

The LOFAR collaboration observes two main fields: the North Celestial Pole (NCP, Yatawatta et al. 2013) and 3C196 (Asad et al. 2015; Ceccotti et al. 2025). The NCP was selected (apart from the benefits due to the location of the interferometer) for its position in a relatively cold spot of the galactic halo, which reduces foregrounds, and because it did not contain an extremely bright source, which results in less artefacts from deconvolution. The 3C196 field was chosen due to its position in a colder region of the galactic halo and due to the presence of a very bright unresolved source located near the centre resulting in accurate direction-independent calibration.

The HERA collaboration, which uses a zenith pointed array, observes various fields throughout a large range of LSTs. Some fields were selected due to minimal diffuse foregrounds and the presence of a bright source from the GLEAM catalogue (Wayth et al. 2015; Abdurashidova et al. 2022). Additional fields were selected to avoid Fornax A and the galactic centre (HERA Collaboration et al. 2023).

More recently, candidate fields have been chosen by Zheng et al. (2020) for the upcoming SKA-Low, using a limited number of parameters to determine field quality, such as minimal galactic emission chosen by cool regions of the Haslam 408 MHz All-Sky map (Haslam et al. 1982), far from the Magellanic clouds, contain minimal bright radio sources that are uniformly positioned within the beam, and should not contain resolved radio diffuse sources. These parameters help to select fields with the intention of making the subsequent post-processing steps (foreground subtraction, calibration, and imaging) easier, and more accurate. Further processing and analysis of one of the candidate fields from this work and several other 'quiet' fields show that selecting a suitable field is critical for EoR science with the SKA (Zheng et al. in preparation).

In this work, we extend those parameters and also extend the number of fields studied. We take both a data-driven and a theoretical approach to this problem to determine the key parameters for determining the quality of a field for EoR science. We use observations of existing fields from the MWA telescope and study the actual calibration precision. We also apply a theoretical approach to predict the most precise calibration that can be obtained for each field. This paper will focus on MWA parameters for characterising fields, but the applicability to the SKA-Low will also be discussed.

This paper is structured as follows: Section 2 goes through the details and process in obtaining data used in this work. Section 3 will discuss the theoretical aspects and desired behaviour of the chosen metrics in this work. Section 4 discusses the theory behind calculating the gain uncertainties. Section 5 describes the computational aspects of the work. In Section 6, we present the results for the extracted metrics and the theoretical gain uncertainties. In Section 7, we discuss and compare the results for the different fields, and finally we conclude the work in Section 8.

2. Data method

2.1 Murchison Widefield Array details

The MWA is a radio interferometer located at the Murchison Radio-astronomy Observatory, a radio quiet zone in Western Australia (Tingay et al. 2013). In this work, we are concerned with the phase II extended configuration (Wayth et al. 2018) of the telescope. This configuration contains 128 tiles with a maximum baseline of approximately 5.2 km. Its operating frequencies are from 70 to 300 MHz, with a field of view of approximately 26 degrees at 150 MHz. The MWA produces data at a spectral resolution of 10 kHz and a temporal resolution of 0.5 s. Each observation is typically 2 min in duration covering only a 30.72 MHz instantaneous bandwidth.

2.2 Data collection and pre-processing

Data were obtained from the MWA ASVO archive[a] through the MWA TAP service. The TAP service was queried with the following settings: observations are within a circle of radius 5° of the phase centre and centred on channel 144 (184.32 MHz, which corresponds to $z \sim 6.8$). With these settings, we obtain observations centred on one of two frequency bands designated for EoR. Furthermore, the settings allow us to obtain as many observations as we can without the sky changing significantly between observations. As mentioned earlier, these observations were made in the Phase II configuration, which allows us to extend upon EoR observations performed by Zheng et al. (2020).

In this work, we inspect the fields used by MWA (EoR0 and EoR1, Barry et al. 2019; Trott et al. 2020; Rahimi et al. 2021), fields which have been used by HERA (Abdurashidova et al. 2022), and fields which were chosen by other metrics (prefixed with 'SKAEOR', Zheng et al. 2020). The phase centres and number of observations for all the fields investigated are given in Table 1. A figure highlighting the fields on the radio sky is given in Figure 1. Due to the use of analogue beamformers in the MWA, the interferometer is only capable of coarse pointing (Tingay et al. 2013). Thus, from the perspective of the MWA, the sky is broken into certain 'grid numbers' (also known as pointing numbers) which describe the pointing. For each field, numerous observations are used in order to separate field-based structure from poor observations (e.g. due to the health of the telescope itself).

Once the data had been downloaded, they were calibrated for direction-independent gains with Hyperdrive[b] (Jordan et al. 2025). The sky model used is a combination of different surveys

---

[a] https://asvo.mwatelescope.org/.

[b] https://github.com/MWATelescope/mwa_hyperdrive.

Table 1. Table of fields which have been downloaded and processed, alongside the right ascension (deg) and declination (deg) of their phase centres. Listed are EoR0 and EoR1 (Lynch et al. 2021), fields used by HERA (Abdurashidova et al. 2022), and fields chosen by other metrics (prefixed with 'SKAEOR', Zheng et al. 2020).

Field name	R.A. (deg)	Dec (deg)	Num. obs.
EoR0	0.00	−30.00	55
EoR1	60.00	−30.00	35
HERA LST 2.0	30.00	−30.00	31
HERA LST 5.2	78.00	−30.00	86
SKAEOR5	118.91	5.86	100
SKAEOR6	128.40	−3.52	26
SKAEOR14	158.14	−12.66	53
SKAEOR15	72.5	−13.35	100

and models, including LoBES (Lynch et al. 2021) for the EoR 0 field, Procopio et al. (2017) for the EoR1 field, Line et al. (2020) for a shapelets model of Fornax A, (Cook, Trott, & Line 2022) for the Centaurus A model and Galactic Plane Supernova Remnants, and the GLEAM survey (Wayth et al. 2015; Hurley-Walker et al. 2016). Only Stokes I information were used for the sky model. We used the brightest 8000 sources. In addition, Hyperdrive uses a per-channel calibration at the resolution of 2 s/40 kHz. Furthermore, Hyperdrive considers the leakage terms in the Jones matrix of the beam response, utilises a simulated Full Embedded Element (FEE) beam model (Sokolowski et al. 2017) and solves for calibration solutions per frequency channel using a similar process described by Mitchell et al. (2008). No antenna flagging algorithms were applied to the data.

Calibration solutions were assessed using the MWA's Quality Analysis pipeline (Nunhokee et al. 2024). Amplitude calibration solutions were normalised to the median, and the phase solutions were also unwrapped before calculating the metrics.

The calibrated visibilities were imaged with WSCLEAN (Offringa et al. 2014). Deconvolution (CLEAN, Högbom 1974) was applied until the data reached the 3σ noise threshold or reached the maximum number of iterations (set to 10 000). Since the field of view of the main lobe of the MWA beam is approximately 21 degrees at 184.32 MHz, we set scale of each pixel to 15 arcsec and the image size to 5 064 × 5 064 pixels.

3. Metrics

This work aims to provide a data-driven approach to selecting ideal fields for EoR science. With this motivation, we will explore the insight and usefulness of a variety of metrics in both the image and calibration space. The metrics to be discussed and their desired behaviour are given in Table 2.

The following sections will first have a brief explanation for the motivation and expected behaviour, followed by more detailed discussion.

3.1 Image metrics

Motivation: Residual signal in peeled images indicates the presence of unmodelled source sidelobe.
Expected behaviour: Root-mean-square noise should be minimised and dynamic range maximised.

In this work, deconvolved multi-frequency synthesis images are produced. Hence, residual signal in these images indicates the presence of unmodelled source sidelobes. The root-mean-square (RMS) and dynamic range (DR) are used to quantify the residual signal. The RMS should be minimised and DR maximised; a high RMS may completely obscure the 21 cm signal and may indicate significant contamination from source sidelobes, while a low DR indicates a lack of bright calibrators or, again, contamination from source sidelobes. The RMS and DR are calculated with the following equations

$$\sigma_{\rm rms} = \sqrt{\frac{1}{N}\sum_{i}^{N} x_i^2} \tag{1}$$

and

$$\chi = \frac{X}{\sigma_{\rm rms}} \tag{2}$$

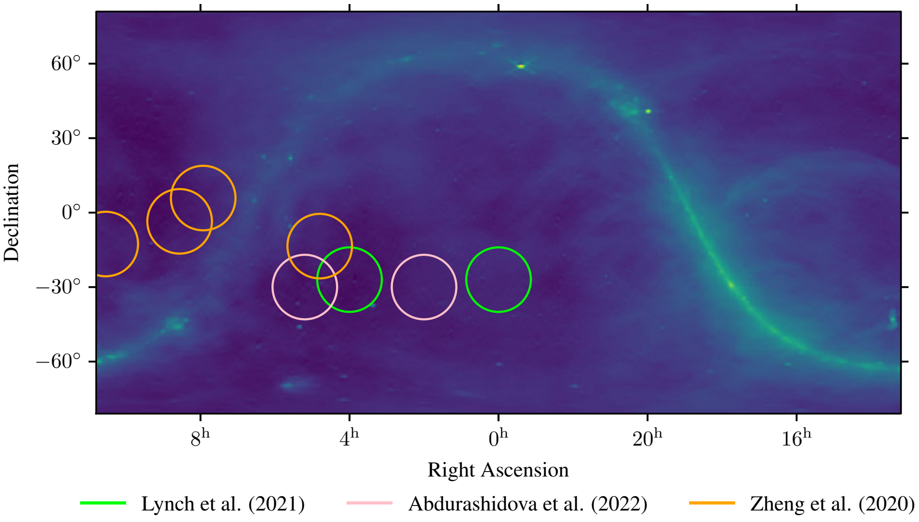

Figure 1. Fields of interest in this study highlighted on the 408 MHz all-sky map (Haslam et al. 1982). Highlighted in green are the MWA EoR1 and EoR2 fields (Lynch et al. 2021). In pink are HERA fields (Abdurashidova et al. 2022). In orange are fields selected by other metrics (Zheng et al. 2020).

Table 2. Table of metrics to be extracted from archival MWA data and their desired behaviour.

Metric	Desired behaviour
Image root-mean-square noise	Low
Image dynamic range	High
Calibration Gain smoothness	Low
Calibration Phase RMSE	Low
Calibration Phase MAD	Low
Calibration Phase Euclidean distance	Low
Calibration Phase KS-metric	Low

respectively, where x_i is the value of each pixel, N is the number of pixels, and X is the value of the brightest pixel.

Deconvolving in the image plane is conceptually related to the process of peeling in the visibility plane: they both aim to remove unwanted sidelobes from the data. The peeling of visibilities is a common step in creating power spectra for EoR science; hence, the RMS of deconvolved images can still be suitable for determining candidate EoR fields. However, in this work, the RMS metric is intended as a simple diagnostic to compare different fields. Therefore, it is most important to ensure consistency in how these images are generated.

3.2 Amplitude solutions smoothness

Motivation: Spectral features in gain amplitudes propagate into final statistics of interest.
Expected behaviour: Smoothness metric should be minimised.

In the calibration solutions case, we investigate the amplitude and phase of the calibration solutions separately. For the amplitude solutions, we inspect the smoothness of the solutions across frequency. The smoothness is especially important since Hyperdrive, our calibration tool, makes no assumptions on how the complex gains should behave; Hyperdrive solves for solutions per-frequency, hence capturing most of the spectral features. In methods that use regularisation, assumptions about how the gains behave are made, and a penalty function is used to constrain the solutions (Ikeda et al. 2025; Yatawatta 2015) which may bias the solutions towards a certain class of solutions.

Amplitude solutions that are not smooth – which may be the result of the particular observing field or an error at the time of observation – can contain spectral structure due to a poor sky model which will propagate into the final power spectrum (Byrne et al. 2019; Ewall-Wice et al. 2017; Barry et al. 2016). This can heavily affect the ability to make a measurement; hence, we suggest that smooth amplitude solutions are ideal. We calculate the smoothness of the amplitude solutions with the following

$$S = \frac{1}{M}\sum_{i=1}^{N_+} m_i, \tag{3}$$

where M is the value of the DC mode of the Fourier transform (FT) of the amplitude solutions, m_i is the value of the i-th positive Fourier mode (after normalising to the median), and N_+ is the number of positive Fourier modes. Since the amplitude solutions are not a periodic signal, we also apply the Blackman–Harris window to reduce spectral leakage (Lessard 2006).

3.3 Phase solutions metrics

Motivation: Phase solutions should be linear and similar between the two polarisations.
Expected behaviour: Root-mean-square error, mean absolute deviation, KS test, and average Euclidean distance should all be minimised.

Hyperdrive applies direction-independent calibration, meaning it calibrates for time delays in the system which arise from factors such as cable lengths from antenna to receiver. A time delay in the signal corresponds to a linear phase shift in Fourier space. Hence, we investigate the linearity of the phase solutions with the root-mean-square-error (RMSE) and mean absolute deviation (MAD). The RMSE and MAD are calculated using the following

$$\mathrm{RMSE} = \sqrt{\frac{1}{N}\sum_{1}^{N}(x_i - \hat{x}_i)^2} \tag{4}$$

and

$$\mathrm{MAD} = \frac{1}{N}\sum_{1}^{N}|r_i - R|, \tag{5}$$

where N is the number of frequency channels, x_i is the antenna's phase solution at frequency channel i, $\hat{x}_i$ is the phase solution predicted by the line of best fit, r_i are the residuals between the observed and predicted phase solutions, and R is the mean value of the residuals.

Another intriguing aspect of the phase solutions arise from the fact that the NS and EW dipoles have differing response patterns. Hence, investigating the similarity between the NS and EW polarisation phase solutions may provide interesting insight in the behaviour of a field. Here, we suggest that solutions which are similar to each other are better than those which are not similar. A dissimilarity can indicate bright sources are present in one polarisation and not the other, or suggest an error occurred during observation in one polarisation. We use two metrics to describe the similarity, the average Euclidean distance between the two sets of solutions, and the Kolgomorov–Smirnov (KS) metric. The Euclidean distance is simply the average of the distance between the NS and EW phase solutions at each channel. A smaller value indicates that the solutions are closer. The KS metric tests how similar the underlying empirical distribution functions of the two sets of solutions are, a value of 0 indicates the two sets are identical while a value of 1 indicates they are the most dissimilar.

4. Theoretical method

In addition to the metrics, a theoretical approach was used to assess the information content of data from different fields and the consequent impact on calibration precision.

4.1 Gain uncertainties

For the theoretical analysis of gain uncertainties, we have used the Crameŕ–Rao bound (CRB) statistic. The CRB provides a lower bound on the variance of an unbiased estimator; or, equivalently, it provides the precision of an unbiased estimator. It does not provide a method for estimating the unknown parameters. The CRB has been used previously to investigate the effects of imprecise calibrator parameters such as the position, spectral index, and brightness (Trott et al. 2011). In this work, the same methods were applied to investigate the best a calibration pipeline can estimate gain uncertainties.

We begin with the Fisher Information Matrix, an element of which can be written in the form (Kay 1993):

$$I_{ab}(\boldsymbol{\theta}) = \frac{2}{\sigma^2}\int \frac{\partial s^H(t;\boldsymbol{\theta})}{\partial \theta_a}\frac{\partial s(t;\boldsymbol{\theta})}{\partial \theta_b}dt, \tag{6}$$

where σ^2 is the variance, $s(t;\boldsymbol{\theta})$ is a signal, H denotes the Hermitian conjugate, and $\boldsymbol{\theta}$ is a vector of unknown parameters which the signal is conditioned on. The signal is given by

$$V_{ab} = \sum_{j=1}^{N_c} B_j g_a \overline{g_b} \exp(-2\pi i(u_{ab}l_j + v_{ab}m_j)), \tag{7}$$

where g_a and g_b are the complex gains of antennas a and b respectively, u_{ab} and v_{ab} are the baseline coordinates between antennas a and b, B_j is the brightness of calibrator j, and l_j and m_j are the calibrator's coordinates (direction cosines). In this study, we have assumed $g_a = g_b = 1$, that is, unity gains.

We are concerned with how well we can estimate the gains g_a and g_b; hence for a telescope with N antennas, we have $\boldsymbol{\theta} = [g_1, g_2, g_3, \ldots, g_N]$. This means $s(t;\boldsymbol{\theta})$ in Equation (6) is a vector of visibilities measured by every baseline. Each element of this vector of length $N_{\text{baselines}}$ is given by Equation (7), where $N_{\text{baselines}} = N^2$ is the number of baselines, including conjugates, and autocorrelations to complete the matrix. Taking the partial derivative of this vector with respect to g_a, we have

$$\frac{\partial s_{ab}(t;\boldsymbol{\theta})}{\partial g_a} = \sum_{j=1}^{N_c} B_j \overline{g_b} \exp(-2\pi i(u_{ab}l_j + v_{ab}m_j)). \tag{8}$$

This means most of the vector, $\frac{\delta s(t;\boldsymbol{\theta})}{\delta g_a}$, will possess a value of 0 and N elements will be populated, since $N_{\text{baselines}} - N$ elements do not contain g_a and will be differentiated to 0.

When $a \neq b$, the product of the two partial derivatives is then only non-zero when the product contains g_a and g_b. For example, for antennas 1 and 2, the product is non-zero when the terms g_1 and g_2 are both present in the product. When $a = b$, the product of the partial derivatives is non-zero at N elements, $N - 1$ of those elements are identical, and 1 element will have a multiplicative factor of 4 due to the partial derivative of a g_a^2 term. Hence, when $a = b$, an additional multiplicative factor of $N + 3$ is needed, this condition can be expressed with a Kronecker-delta function. The final expression for an element of the Fisher Information Matrix is

$$I_{ab}(\boldsymbol{\theta}) = (N+3)^{\delta_{ab}} \times \frac{2}{\sigma^2} \times \int \sum_{j=1}^{N_c}\sum_{k=1}^{N_c} B_j B_k g_a \overline{g_b} \exp\left\{-2\pi i(u_{ab}(l_j - l_k) + v_{ab}(m_j - m_k)\right\}dt. \tag{9}$$

The variance σ^2 of a single visibility signal measured by a single baseline is given by

$$\sigma = \frac{2k_b T_{\text{sys}}}{A_{\text{eff}}\sqrt{\Delta\nu\Delta\tau}}, \tag{10}$$

where k_b is the Boltzmann constant, T_{sys} is the system temperature, A_{eff} is the effective area of an antenna, $\Delta\nu$ is the bandwidth of a single measurement, and $\Delta\tau$ is the integration time for a single measurement.

The CRB matrix is then the inverse of Equation (9), and the gain uncertainties can be found on the square root of the diagonal of this matrix. Previous work with the CRB (Trott et al. 2011) has shown one bright calibrator produces better gain and phase precision compared to many lower brightness sources.

4.2 Propagation of gain uncertainties

To propagate gain uncertainties into the visibilities, we use the standard covariance matrix method given by

$$\sigma^2_{V_{ab}} = \left[\mathbf{J}\mathbf{C}_\theta\mathbf{J}^\dagger\right]_{ab}, \tag{11}$$

where $\mathbf{J}$ is the Jacobian of partial derivatives of the visibility function with respect to the parameters $\theta_{ab} = (g_a, g_b)$, $\mathbf{J}^\dagger$ is the complex conjugate, and $\mathbf{C}_\theta$ is the covariance matrix of parameter uncertainties. Expanding out Equation (11), we arrive at the following

$$\sigma^2_{V_{ab}} = \left|\frac{\partial V_{ab}}{\partial g_a}\right|^2 \sigma^2_{g_a} + \frac{\partial V_{ab}}{\partial g_a}\overline{\frac{\partial V_{ab}}{\partial g_b}}\text{cov}_{g_b g_a} + \overline{\frac{\partial V_{ab}}{\partial g_a}}\frac{\partial V_{ab}}{\partial g_b}\text{cov}_{g_a g_b} + \left|\frac{\partial V_{ab}}{\partial g_b}\right|^2 \sigma^2_{g_b}, \tag{12}$$

and since we assume the gains are unity, meaning the coefficients of the variance and covariance terms are the same, this expression can be simplified further to

$$\sigma^2_{V_{ab}} = \left|\frac{\partial V_{ab}}{\partial g_a}\right|^2 (\sigma^2_{g_a} + cov_{g_a g_b} + cov_{g_b g_a} + \sigma^2_{g_b}). \tag{13}$$

The variance and covariance terms can be directly taken from the diagonal and off-diagonals of the CRB matrix, respectively.

5. Computational method

5.1 Metrics

The evaluation of both the image and most of the calibration metrics is simple. Equations (1) and (2) were evaluated after reading in the image data. The smoothness of the amplitude solutions of the antenna were found by evaluating Equation (3), after applying a Blackman–Harris window to the solutions. The phase linearity metrics were evaluated for each set of phase solutions by first applying a linear fit to the data and then evaluating Equations (4) and (5). The Euclidean distance was simply the average of the absolute value of the difference between the NS and EW phase solutions at each channel, and the KS metric was obtained using the `kstest` method from `scipy` (Virtanen et al. 2020).

5.2 Detecting metric outliers

It is inevitable that some observational data are corrupted by some source of error that is independent of the sky, such as problems with the telescope or strong Radio Frequency Interference (RFI). For this work, these effects need to be disentangled from sky-based effects. Processing these bad observations will result in outliers in the metrics. These outliers were detected by first treating each observation's metrics as a 128-dimensional point and then calculating the distance to every other observation's metrics (another 128-dimensional point). We then calculate the MAD for these distances to use in the modified z-score. In this paper, a threshold of 5σ was used to determine if a result is an outlier. The number of observations left after applying this method for each field is given in Table 3.

Table 3. Number of 2-min observations per field remaining after bad data have been removed with the method described in Section 5.2.

Field name	Num. observations
EoR0	39
EoR1	25
HERA LST 2.0	19
HERA LST 5.2	63
SKAEOR5	65
SKAEOR6	21
SKAEOR14	28
SKAEOR15	68

5.3 Gain uncertainties

In this work, all simulations are zenith pointed meaning simulations of some of the fields may not be representative of reality, as some fields do not transit the zenith of the MWA. However, this allows us to compare the effects of source positions within the beam between the different fields. Furthermore, it is common to calibrate only with sources within the main lobe of the primary beam, because these are the most reliable. Hence, during these calculations, only sources within the main lobe are preserved. The main lobe will change slightly depending on pointing, but overall it will behave similarly whether at zenith or off-zenith. Therefore, simulating at zenith will still provide valuable insight while allowing for much easier implementation.

Additionally, all components in the sky model are treated as point sources in the simulation, as Equation (9) requires only the brightness and positions of the sources. This means that Fornax A, which is composed of shapelets in our sky model, is modelled as a set of point sources with large brightness. Moreover, systematics like sky model uncertainties are unaccounted for; all other parameters are assumed to be accurate.

Equation (10) was first evaluated for the given input parameters. In this work, the values used are representative of EoR science with the MWA telescope $T_{\mathrm{sys}} = 200$ K (value at the centre of the bandwidth), $N = 128$, $A_{\mathrm{eff}} = 21\ \mathrm{m}^2$, $\Delta\nu = 80$ kHz, and $\Delta\tau = 8$ s. The field of view of a telescope can be approximated with $\theta \approx \frac{\lambda}{D}$ where D is the diameter of a dish/antenna. For the MWA, $D = 4.4$ m. We have assumed that A_{eff} does not change with frequency (Tingay et al. 2013).

Next, the calculation and propagation of the gain uncertainties takes place within a large loop over the frequency range. At the beginning of each iteration, sources in the sky model were vetoed by the current field of view and also their estimated flux density for that frequency. Following this, the beam pattern is calculated for the current frequency, using the array factor method (Warnick et al. 2018), in a 1 024 by 1 024 grid where each pixel corresponds to a portion of the sky in the (l, m) plane. These pixel values are used to attenuate sources located within the pixel by simply multiplying the source brightness by the pixel value.

The attenuated sources are then used to calculate the CRB matrix by first generating the FIM matrix with Equation (9), where each element represents an antenna pair (a, b). The FIM is Hermitian; hence, only the top triangle of the matrix needs to be calculated and the bottom triangle can be filled in by taking the complex conjugate. The CRB are the diagonal elements of the inverse of the FIM matrix, and the gain uncertainties for each antenna are their square root.

5.4 Power spectra

Taking the previously calculated gain uncertainties, still within the large frequency loop, the uncertainties for visibilities were evaluated with Equation (13). Once uncertainties were calculated, the real and complex components for the visibilities for each baseline were randomly generated from a normal distribution with mean 0 and standard deviation $\frac{\sigma_{V_{ab}}}{\sqrt{2}}$. The visibilities were then gridded onto a common (u,v) grid and appended onto a growing list of gridded visibilities.

Once the loop completed, we were left with a data cube of gridded visibilities at each frequency channel. To transform this data cube into the final power spectrum, a FT was applied to each (u,v) cell along the frequency axis. The result was then multiplied by its complex conjugate to yield the unnormalised power. We then cylindrically average the unnormalised power at each η slice (the FT of frequency) to arrive at the 2D temperature power spectrum.

6. Results

This section will present the results of the calculations and attempt to provide explanations for the behaviour seen in some metrics. The information gained and the usefulness of the metrics will also be discussed. All results shown are generated after applying the threshold technique discussed in Section 5.2. Outliers in this study generally stem from either computational errors or bad data, not from the behaviour of the fields. Differences between NS and EW polarisations arise from their different fringe patterns. In this section, we display results only for the EoR0 field as an indicative field; results for the other fields can be found in the appendices. The following metrics were found to be most useful: image RMS and dynamic range, amplitude smoothness, and phase RMSE.

6.1 Image metrics

The RMS and dynamic range of the EoR0 field can be found in Figure 2. Both the RMS and DR of the fields can be seen varying with the observation ID for a particular pointing. This behaviour could be due to sources moving in and out of the main/side lobes of the MWA with observation ID. Although these metrics are displayed in increasing observation ID, it does not necessarily mean successive points are observations performed immediately after each other.

6.2 Amplitude solutions smoothness

The smoothness of both NS and EW polarisation amplitude calibration solutions for EoR0 can be found in Figure 3. Some fields exhibit clustering between lines of different observations IDs, and this is especially prominent in the HERA LST 2.0 field in the NS amplitude smoothness found in Appendix B. This clustering behaviour could be explained by different conditions at the time of observation or, simply, an insufficient amount data to provide a robust representation of the field.

For a simplified version of the same data, a band plot of the same EoR0 data in Figure 3 is given in Figure 4, plotted in this

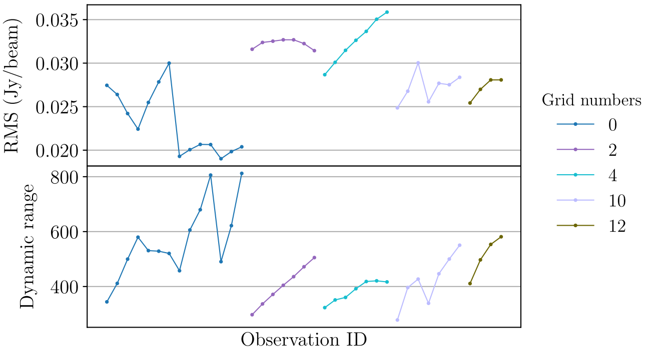

Figure 2. Image metrics for the EoR0 field grouped by pointing (represented by different colours) for observation IDs in ascending order. The top panel shows the root mean square (RMS) metric. The bottom panel shows the dynamic range metric. The changing values between observations are due to sources moving in and out of the MWA beam metric.

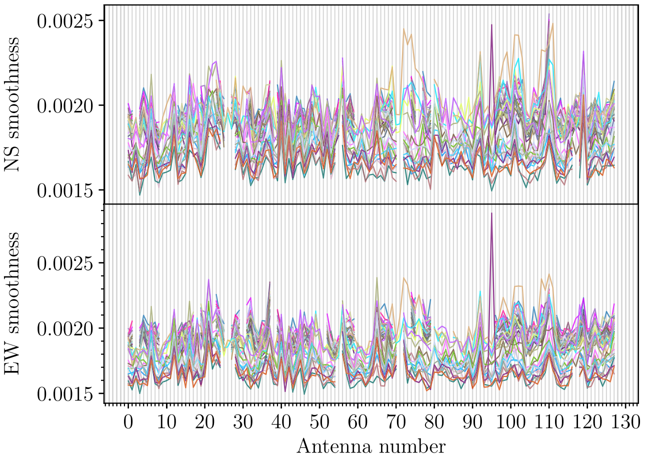

Figure 3. Smoothness of the NS (top) and EW (bottom) calibration amplitude solutions for EoR0 for each antenna. Each line represents a different observation ID. A smaller value represents smoother amplitude solutions.

figure are the median (red line), and the lower and upper quartiles (shaded region).

To showcase the smoothness metric, the NS amplitude solutions are given for observation 1201153128 at antennas 100 and 110 in Figure 5. From Figure 4, we can see that, generally, antenna 110 amplitude solutions are less smooth than the solutions of antenna 100. Indeed, this is the observed behaviour in Figure 5.

6.3 Phase solutions metrics

The RMSE metrics for EoR0 are displayed in Figure 6. In this metric, a smaller number corresponds to a more linear phase solution. We once again observe similar clustering behaviour in some of these results. However, it appears that behaviour that is present in the amplitude calibration solutions does not necessarily translate to the phase metrics. The MAD behaves almost identically to the RMSE; hence, moving forward we focus on the RMSE metric.

Finally, the average Euclidean distance metrics for the EoR0 field are given in Figure 7. It is challenging to glean any information from the two similarity metrics; in particular, the KS metric seems to be the most random of all the metrics. For that reason, we will continue without KS metric. However, in the average Euclidean distance metric, some fields do exhibit clustering behaviour. For example, the EoR0 field appears to have two distinct groupings of average distances, where one group is more similar than the other. Although it does exhibit more behaviour than the KS metric, we opt to move without this metric going forward, as it is still difficult to obtain useful information.

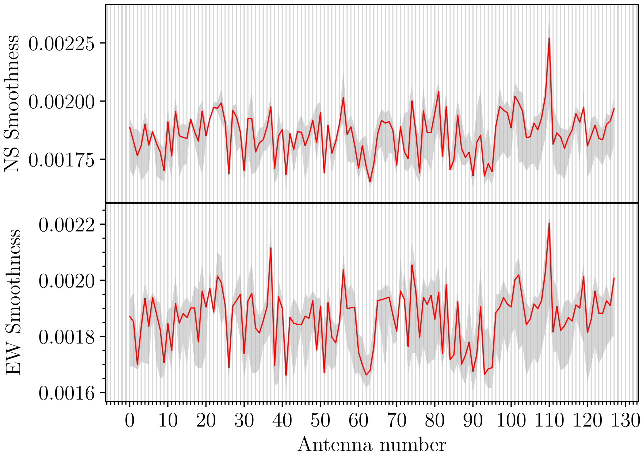

Figure 4. Band plot of the smoothness of the NS (top) and EW (bottom) amplitude calibration solutions for EoR0 for each antenna. The median per antenna is given in red, and the upper and lower quartiles per antenna are given by the shaded region. A smaller value represents smoother amplitude solutions.

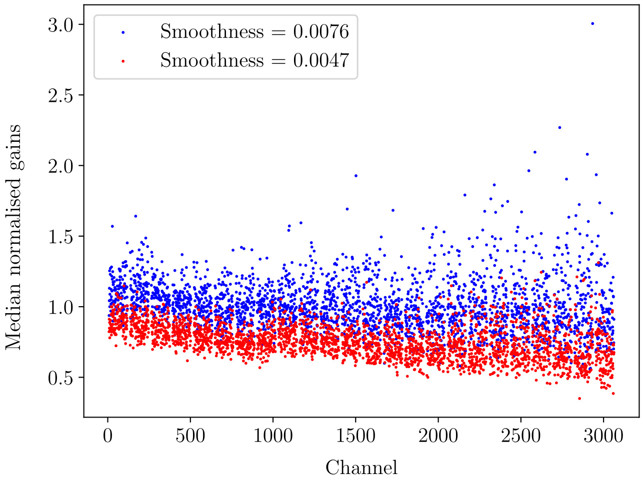

Figure 5. Calibration amplitude solutions for antenna 100 (red points) and antenna 110 (blue points) of observation 1201153128. A lower smoothness metric corresponds to visually smoother amplitudes. Indeed, we see that the antenna 100 (smoothness = 0.0047) is visually smoother then antenna 110 (smoothness = 0.0076).

6.4 Smoothness and RMSE correlations

The NS smoothness and RMSE correlation plot for the EoR0 field can be found in Figure 8. In this figure, each colour and marker combination indicates an individual observation. Each point is described by the antenna's smoothness and RMSE metrics, and the opacity of the point relates to the antenna number. The more opaque points correspond to the long baseline tiles. In this figure, we can see for observations below RMSE=8, there exists a correlation between the smoothness and RMSE metric. As the amplitude solutions become less smooth (increasing smoothness metric),

https://doi.org/10.1017/pasa.2025.10100

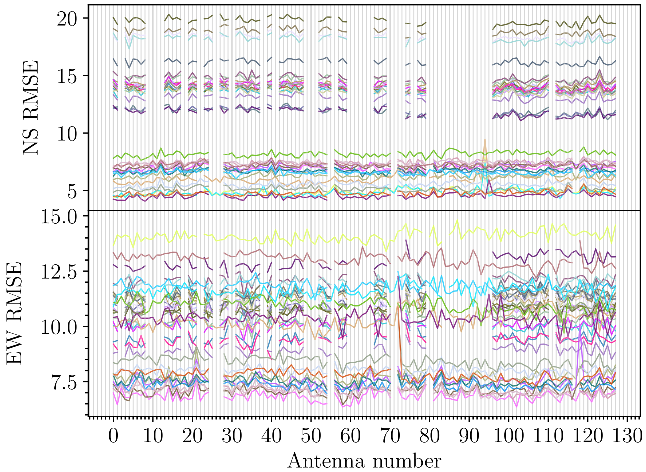

Figure 6. Root-mean-square-error metric of both NS (top) and EW (bottom) calibration phase solutions for observations of the EoR0 field. Each line represents a different observation ID. A smaller value represents a more linear phase solution.

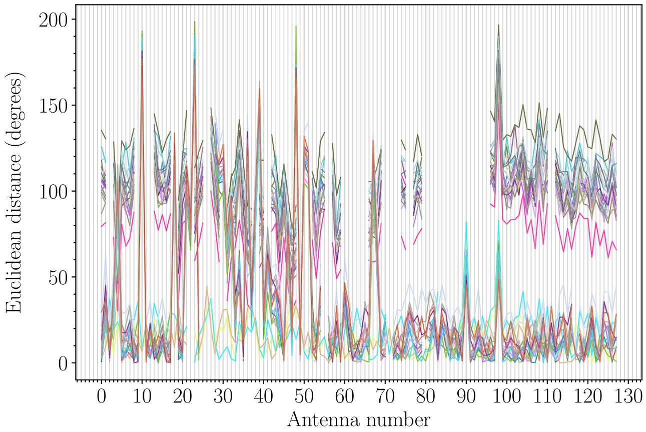

Figure 7. The average Euclidean distance metric between NS and EW calibration phase solutions for the EoR0 field. Each line represents a different observation ID. A lower value represents more similar phase solutions. In this field, there appears to be two groupings of distances where one group describes very similar phase solutions.

the RMSE metric also increases. This trend seems to flatten off for observations above RMSE=8 in the EoR0 field. Results for other fields, although not exactly the same shape, all show there is a positive correlation between these two metrics.

It is also worth noting in Figure 8 the clustering of observations with grid number 0 around RMSE values of 7, 12, and 14. A table of LSTs and start dates in UTC for observations with grid number 0 are given in Table 4. The cause of this clustering behaviour seem to stem from conditions at the time of observation and how close the observations are in terms of time.

6.5 Theoretical gain uncertainties

The theoretical gain uncertainties for each field as a function of antenna number can be found in Figure 9. A combined histogram of the source brightness in each field is given in Figure 10, and the number of sources in each field along with the brightest source is given in Table 5. The three fields that produce the best gain uncertainties via the CRB matrix are SKAEOR15, EoR1, and HERA LST 5.2. These three fields show that having bright sources and a large number of points increase the gain precision.

Table 4. Table of EoR0 observations with a grid number 0. The LST and start date in UTC are included for each observation. There are at least two large groups of observations which are close in time, while the others form smaller groups. These groupings could provide an explanation for the clustering of observations seen in Figure 8.

Observation ID	LST	Start date (UTC)
1286204984	361.98	2024-09-24T10:47:08
1286203784	356.97	2024-09-24T10:48:58
1286205584	364.49	2024-09-24T10:46:57
1286806936	356.98	2024-09-24T10:46:54
1286807536	359.49	2024-09-24T09:43:57
1194267224	358.92	2024-09-24T13:09:09
1194266984	357.91	2024-09-24T13:12:29
1286808736	364.50	2024-09-24T09:29:54
1194267464	359.92	2024-09-24T13:05:15
1286204384	359.48	2024-09-24T10:48:50
1194267704	0.92	2024-09-24T13:02:45
1194266744	356.91	2024-09-24T13:15:29
1194267944	1.92	2024-09-24T12:00:17
1194268184	2.93	2024-09-24T11:54:31

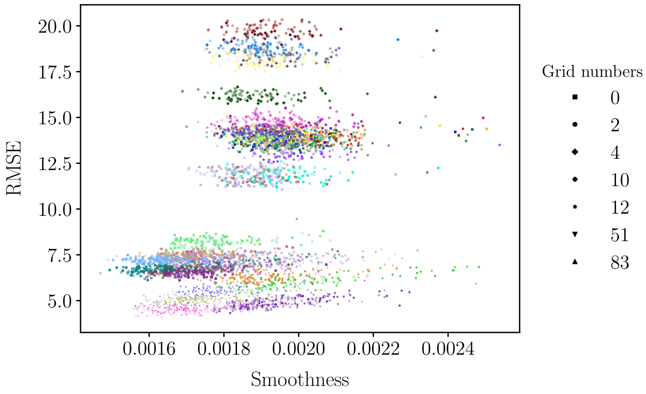

Figure 8. Plot displaying the correlation between the calibration amplitude smoothness metric and the NS calibration phase root-mean-square-error (RMSE) metric for observations of the EoR0 field. There is a positive correlation between the two metrics and seems to flatten off at higher RMSE values. Also seen is clustering of the observations with grid number 0, at RMSE values of 7, 12, and 14.

The power spectra for each field, after propagating these theoretical uncertainties into the visibilities, can be found in Figure 11. Interestingly, fields which have shown better theoretical calibration solutions previously do not have the best performing power spectra. This can be explained by considering Equation (13), the partial derivative coefficient is dependent on the brightness of the sources selected by the simulation. Hence, even if the gain uncertainties may be better for a particular field, they are imprinted upon the brightest sources in the field which may mean the power spectrum overall performs worse in comparison to other fields.

A 2D power spectrum for a pure 21 cm signal from a 'faint galaxies' model (de-projected from a 1D spherically averaged power spectrum, Mesinger, Greig, & Sobacchi 2016) is given in Figure 12. The theoretical power spectra of this work are at least an order of magnitude larger than the predicted signal.

Table 5. Table of the number of sources within the field of view of the beam and the brightest source at 182 MHz during the Cramer-Rao bound calculation, for each field. This table helps us reveal how the number of sources, and the brightest source result in the gain uncertainties we see in Figure 9.

Field name	Number of sources	Brightest source (Jy)
EoR0	241	19.3
EoR1	233	32.4
HERA LST 2.0	170	16.2
HERA LST 5.2	220	50.0
SKAEOR5	219	23.3
SKAEOR6	240	23.3
SKAEOR14	170	8.6
SKAEOR15	274	14.2

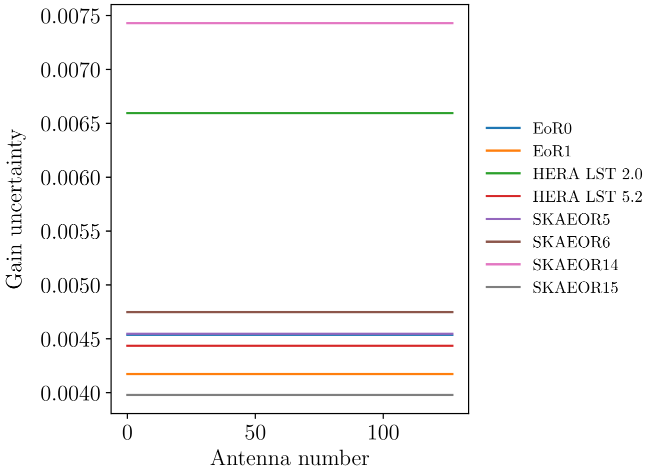

Figure 9. Theoretical gain uncertainties of various fields for 128 MWA antennas in the phase II configuration at 182 MHz, calculated with the procedure described in Section 5.3. Each field were treated as being zenith pointed. There are miniscule fluctuations between antennas for all fields.

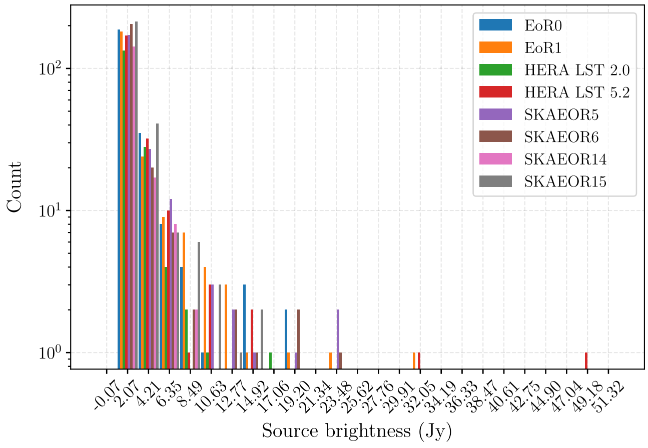

Figure 10. Combined histogram of source brightness for each field at 182 MHz during the Cramer-Rao bounds calculation. The width of each bin is 2.14 Jy. This histogram, along with Table 5, help to investigate how the distribution of source brightness result in the gain uncertainties seen in Figure 9.

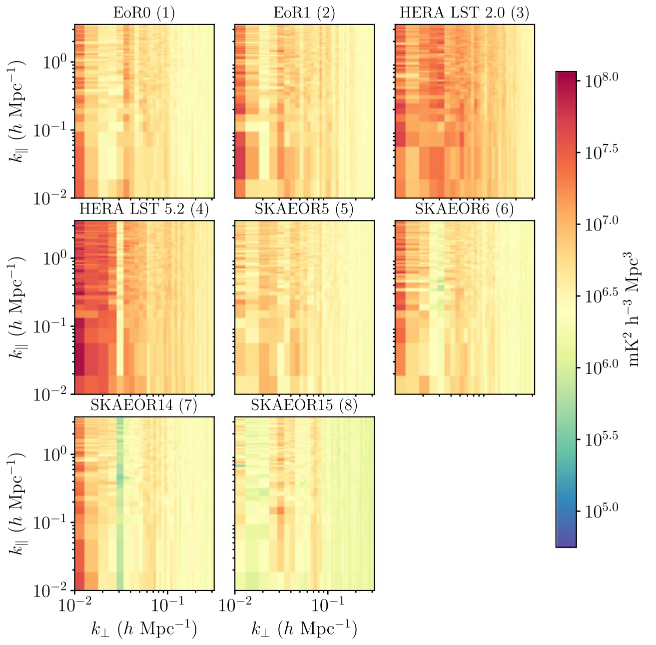

Figure 11. Resulting power spectra for each field after propagating theoretical uncertainties into visibilities. Each field was treated as if it were at zenith.

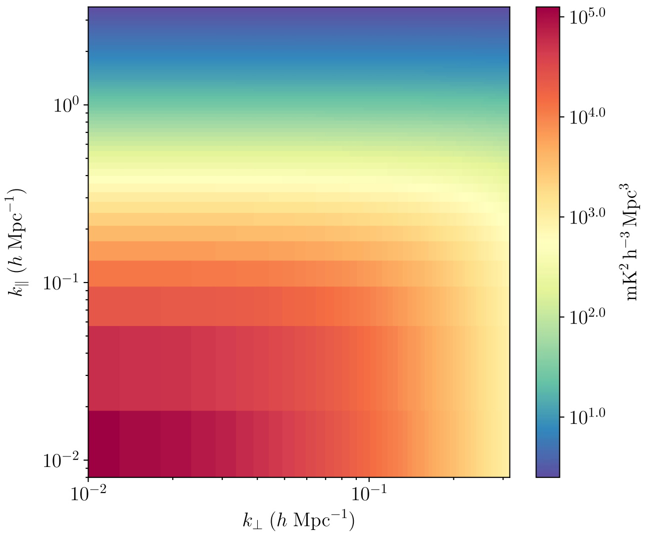

Figure 12. A 2D power spectrum of a pure 21 cm signal from a 'faint galaxies' simulation (Mesinger et al. 2016) centred on $z \sim 7$.

7. Discussion

Having displayed the metrics and the theoretical analysis, we will attempt to select a few fields that may be ideal for EoR science. We will first begin by disentangling telescope-based effects from sky-based effects. Hence, our first criteria will be the number of observations available per field. This leaves us with four fields, and these fields are EoR0, HERA LST 5.2, SKAEOR5, and SKAEOR15. Within these fields, we inspect the average behaviour of the metrics, not the antenna to antenna or observation to observation behaviour, which should be uncorrelated. Figures for image metrics of the other metrics can be found in Appendix A, amplitude

Table 6. Table of the four fields for consideration as an EoR observing field, and their relative performance to each other in the metrics used in this work. Performance was determined visually based on desired behaviours as described in Table 2. A check mark (✓) indicates the respective field(s) perform well in that metric, a tilde (~) indicates reasonable performance, and a cross (×) indicates bad performance.

	Metrics					
Field	Image RMS	Image DR	XX Amp. smoothness	YY Amp. smoothness	XX Phase RMSE	YY Phase RMSE
EoR0	✓	✓	~	~	×	✓
HERA LST 5.2	×	✓	✓	✓	✓	×
SKAEOR5	~	~	×	×	×	×
SKAEOR15	×	×	×	×	~	✓

smoothness in Appendix B and Appendix C, phase RMSE in Appendix D, and average Euclidean distance in Appendix E.

Next, we narrow down the selection based on the performance of these four fields in the metrics. Table 6 displays how the fields compare relative to each other, where the comparison of metrics was a simple visual inspection. From this table, we can immediately exclude SKAEOR5 and SKAEOR15 from our selection, leaving only the EoR0 and HERA LST 5.2 fields.

Introducing the power spectra now will further narrow down the selection. To serve as a reminder, these power spectra showcase the impact of gain uncertainties due to the calibrators' positions within the beam. They also simulate a zenith pointing; hence, simulations of these fields are not completely physical. Additionally, due to the sky model used in this study, some parts of the sky are better modelled than others.

With these factors in mind, from Figure 11 it is clear that the HERA LST 5.2 field is most affected by the gain uncertainties. The other three fields are EoR0, SKAEOR5, and SKAEOR15 and display acceptable impacts from gain uncertainties. However, in reality, the SKAEOR5 field has a very northern declination, where the beam of the MWA starts to misbehave. Taking everything into account, the EoR0 field seems to be a safe field for observation.

We must also discuss the applicability of these metrics, which were calculated using archived MWA data, to the SKA-Low telescope. SKA-Low will have a much smaller field-of-view, $\sim 2.5^\circ$ as opposed to $\sim 2.5^\circ$ at 184.32 MHz, along with better sensitivity than the MWA. To compare the number of sources that would be detected by the MWA and SKA-Low, we can investigate the ratio of the integrated source counts, $\frac{N_{\rm SKA}}{N_{\rm MWA}}$. The integrated source count is given by

$$N(S > S_{\rm min}) = \frac{\alpha}{1-\beta}\left(\frac{S_{\rm min}}{S_0}\right)^{1-\beta}\Omega, \tag{14}$$

where α and β are fitting parameters that are intrinsic to the sky. The FOV, Ω, can be approximated by $\frac{\lambda}{D}$, where D is the diameter of an MWA tile or SKA station. $S_{\rm min}$ is the sensitivity of the MWA or SKA is given by Equation (10). In this section, we express the sensitivity in the form

$$S_{\rm min} = \frac{\rm SEFD}{\sqrt{\Delta\nu\Delta\tau}\sqrt{N_b}}, \tag{15}$$

where $\Delta\nu$, $\Delta\tau$, and N_b are the bandwidth, integration times, and number of baselines, respectively. The SEFD is calculated using

$${\rm SEFD} = \frac{2kT_{\rm sys}}{A_e}, \tag{16}$$

where k is the Boltzmann constant and A_e is the effective collecting area. The ratio of SKA integrated source counts to MWA integrated source counts is given by

$$\frac{N_{\rm SKA}}{N_{\rm MWA}} = \left(\frac{{\rm SEFD}_{\rm SKA}\sqrt{N_{b,\rm MWA}}}{{\rm SEFD}_{\rm MWA}\sqrt{N_{b,\rm SKA}}}\right)^{1-\beta}\frac{D_{\rm MWA}}{D_{\rm SKA}}, \tag{17}$$

where $D_{\rm SKA}$ and $D_{\rm MWA}$ are the diameters of an SKA station and MWA tile, respectively (approximately 38m for the SKA and 4.4m for the MWA). For both SKA and MWA, we assume $T_{\rm sys} \approx 200$ K at 150 MHz. The effective collecting area of the MWA at 150 MHz is $A_{e,\rm MWA} = 21.5\ {\rm m}^2$, for the SKA we will assume a single SKA station is 100% efficient resulting in $A_{e,\rm SKA} = 1134.11\ {\rm m}^2$. The system equivalent flux densities are then ${\rm SEFD}_{\rm MWA} \approx 25\,000$ Jy and ${\rm SEFD}_{\rm SKA} \approx 500$ Jy. In this calculation, we use the source counts of Intema et al. (2011) to obtain $\beta = 1.59$. The number of unique baselines for SKA-Low and MWA are $N_{b,\rm SKA} = 131\,086$ and $N_{b,\rm MWA} = 8128$. With these values, Equation (17) is evaluated to approximately $\frac{N_{\rm SKA}}{N_{\rm MWA}} \approx 0.5$.

The SKA-Low will approximately detect half of what the MWA can detect, with the better sensitivity and smaller field of view. The effects of this will be difficult to discuss with certainty. But since we have shown a dependence on the number of sources and in particular the brightest sources, fields with bright sources near zenith in both the SKA and MWA field of view can be expected to behave similarly. Additionally, there is a dependence on the number of antennas in Equation (9). The combined effects of these dependencies is difficult to predict.

In the image metrics with SKA-Low, we can expect lower RMS and larger dynamic range (if a bright source is within the field of view) due to the increased sensitivity of SKA-Low. The calibration metrics are more challenging to estimate. We have seen with the HERA LST 5.2 simulation (which, in reality, is a zenith field) that the bright source contributes to a lower uncertainty, which is then reflected in the NS and EW amplitude smoothness metrics. Considering the correlation between amplitude smoothness and phase RMSE, we can further reason that the phase solutions should also be linear. Of course, this line of reasoning is only applied for the HERA LST 5.2 field and may not hold for other fields. Recently, work from LOFAR which uses a 6-h observation of their target field containing 3C196 (Ceccotti et al. 2025), a very bright source near zenith, has seen lower systematics compared to the colder NCP field. This aligns with the behaviour we have explored in this work. We do not apply additional steps in the power spectrum estimation; hence, we cannot compare the power spectra of this work with those of the recent LOFAR work.

SKA-Low will also have the ability to form multiple beams and utilise sub-stations. It will also use digital beam formers which will allow for greater pointing precision. Further investigation into how these variables will affect EoR observations will be needed.

8. Conclusion

In this study, we have investigated image metrics (RMS and dynamic range) and calibration metrics (amplitude smoothness, RMSE of the phase solutions, and average Euclidean distance between the phase solutions of different polarisations). We utilised archival MWA data in the phase II configuration centred on 184.32 MHz ($z \sim 6.8$), with observations pointing towards fields used by the MWA collaboration (Lynch et al. 2021), HERA team (Abdurashidova et al. 2022), and fields previously chosen by other metrics (Zheng et al. 2020). These data were used as a proxy for future SKA-Low data. We found the most useful metrics to be the image RMS, dynamic range, amplitude smoothness, and phase RMSE.

In addition to the metrics, a theoretical method utilising the CRB was used to calculate theoretical gain uncertainties. A standard error propagation of these uncertainties into the final power spectrum was also provided. From this, we have seen that the brightest sources contribute the most to a lower gain uncertainty.

The combination of both metrics and theoretical power spectra helped to confirm that EoR0 is indeed a candidate for future EoR observations. In particular, the field's performance in the both image metrics, and its impacts on the final power spectrum – while also being a real pointing used by the MWA – has led us to this conclusion. However, this shouldn't dissuade the investigation of the other fields. The HERA LST 5.2 field was shown to perform well in the smoothness metric, which aligns with behaviour in recent work from LOFAR (Ceccotti et al. 2025). Additionally, the HERA LST 5.2 field has the largest dynamic ranges (but also large RMS) out of the fields discussed. The SKAEOR5 field, which contains the second-largest number of observations, has a slowly varying image RMS second to the EoR0 RMS. Clearly, these fields are still worth investigating.

Acknowledgement. This research was partly supported by the Australian Research Council Centre of Excellence for All Sky Astrophysics in 3 Dimensions (ASTRO 3D), through project number CE170100013. The International Centre for Radio Astronomy Research (ICRAR) is a Joint Venture of Curtin University and The University of Western Australia, funded by the Western Australian State government. This scientific work uses data obtained from *Inyarrimanha Ilgari Bundara*/the Murchison Radio-astronomy Observatory. We acknowledge the Wajarri Yamaji People as the Traditional Owners and native title holders of the Observatory site. Establishment of CSIRO's Murchison Radio-astronomy Observatory is an initiative of the Australian Government, with support from the Government of Western Australia and the Science and Industry Endowment Fund. Support for the operation of the MWA is provided by the Australian Government (NCRIS), under a contract to Curtin University administered by Astronomy Australia Limited. This work was supported by resources provided by the Pawsey Supercomputing Research Centre with funding from the Australian Government and the Government of Western Australia.

References

Abdurashidova, Z., et al. 2022, ApJ, 925, 221. https://doi.org/10.3847/1538-4357/ac1c78. arXiv: 2108.02263 [astro-ph.CO].

Acharya, A., Mertens, F., Ciardi, B., Ghara, R., Koopmans, L. V. E., & Zaroubi, S. 2024, MNRAS, 534, L30. issn: 1745-3933. https://doi.org/10.1093/mnrasl/slae078.

Asad, K. M. B., et al. 2015, MNRAS, 451, 3709. https://doi.org/10.1093/mnras/stv1107. arXiv: 1503.01644 [astro-ph.CO].

Barry, N., Hazelton, B., Sullivan, I., Morales, M. F., & Pober, J. C. 2016, MNRAS, 461, 3135. issn: 1365-2966. https://doi.org/10.1093/mnras/stw1380.

Barry, N., et al. 2019, ApJ, 884, 1. issn: 1538-4357. https://doi.org/10.3847/1538-4357/ab40a8.

Bowman, J. D., & Rogers, A. E. E. 2010, Natur, 468, 796. issn: 1476-4687. https://doi.org/10.1038/nature09601.

Brackenhoff, S. A., et al. 2025, MNRAS, 541, 3993. issn: 1365-2966. https://doi.org/10.1093/mnras/staf1206.

Byrne, R., et al. 2019, ApJ, 875, 70. issn: 1538-4357. https://doi.org/10.3847/1538-4357/ab107d.

Ceccotti, E., et al. 2025, https://doi.org/10.48550/ARXIV.2504.18534.

Chapman, E., & Jelic, V. 2019, in The Cosmic 21-cm Revolution (IOP Publishing). isbn: 9780750322348. https://doi.org/10.1088/2514-3433/ab4a73ch6.

Chokshi, A., Barry, N., Line, J. L. B., Jordan, C. H., Pindor, B., & Webster, R. L. 2024, MNRAS, 534, 2475. issn: 1365-2966. https://doi.org/10.1093/mnras/stae2264.

Cook, J. H., Trott, C. M., & Line, J. L. B. 2022, MNRAS, 514, 790. https://doi.org/10.1093/mnras/stac1330. arXiv: 2205.04644 [astro-ph.CO].

DeBoer, D. R., et al. 2017, PASP, 129, 045001. issn: 1538-3873. https://doi.org/10.1088/1538-3873/129/974/045001.

Eastwood, M. W., et al. 2019, AJ, 158, 84. issn: 1538-3881. https://doi.org/10.3847/1538-3881/ab2629.

Ellingson, S. W., Clarke, T. E., Cohen, A., Craig, J., Kassim, N. E., Pihlstrom, Y., Rickard, L. J., & Taylor, G. B. 2009, Proc. IEEE, 97, 1421. issn: 1558-2256. https://doi.org/10.1109/jproc.2009.2015683.

Ewall-Wice, A., Dillon, J. S., Liu, A., & Hewitt, J. 2017, MNRAS, 470, 1849. issn: 1365-2966. https://doi.org/10.1093/mnras/stx1221.

Furlanetto, S. R., Peng Oh, S., & Briggs, F. H. 2006, PhyR, 433, 181. issn: 0370-1573. https://doi.org/10.1016/j.physrep.2006.08.002.

Haslam, C. G. T., Salter, C. J., Stoffel, H., & Wilson, W. E. 1982, A&AS, 47, 1.

HERA Collaboration, et al. 2023, ApJ, 945, 124. https://doi.org/10.3847/1538-4357/acaf50. arXiv: 2210.04912 [astro-ph.CO].

Högbom, J. A. 1974, A&AS, 15, 417.

Hurley-Walker, N., et al. 2016, MNRAS, 464, 1146. issn: 1365-2966. https://doi.org/10.1093/mnras/stw2337.

Ikeda, S., Nakazato, T., Tsukagoshi, T., Takeuchi, T. T., & Yamaguchi, M. 2025, PASJ, 77, 260. issn: 2053-051X. https://doi.org/10.1093/pasj/psae114.

Intema, H. T., vanWeeren, R. J., Röttgering, H. J. A., & Lal, D. V. 2011, A&A, 535, A38. issn: 1432-0746. https://doi.org/10.1051/0004-6361/201014253.

Jacobs, D. C., et al. 2016, ApJ, 825, 114. issn: 1538-4357. https://doi.org/10.3847/0004-637x/825/2/114.

Jordan, C., et al. 2025, in Proceedings of the 7th URSI Asia-Pacific Radioscience Conference – AP-RASC 2025. URSI AP-RASC 2025. URSI – International Union of Radio Science. https://doi.org/10.46620/ursiaprasc25/lscn1310.

Kay, S. M. 1993, Fundamentals of Statistical Signal Processing: Estimation Theory (Prentice-Hall).

Koopmans, L., et al. 2015, in Proceedings of Advancing Astrophysics with the Square Kilometre Array – pos(aaska14). AASKA14. Sissa Medialab. https://doi.org/10.22323/1.215.0001.

Lessard, C. S. 2006, in Signal Processing of Random Physiological Signals (Springer International Publishing), 175. isbn: 9783031016103. https://doi.org/10.1007/978-3-031-01610-3_16.

Line, J. L. B., et al. 2020, PASA, 37. issn: 1448-6083. https://doi.org/10.1017/pasa.2020.18.

Lynch, C. R., et al. 2021, PASA, 38. issn: 1448-6083. https://doi.org/10.1017/pasa.2021.50.

Mertens, F. G., et al. 2020, MNRAS, 493, 1662. https://doi.org/10.1093/mnras/staa327. arXiv: 2002.07196 [astro-ph.CO].

Mertens, F. G., et al. 2025, A&A, 698, A186. https://doi.org/10.1051/0004-6361/202554158. arXiv: 2503.05576 [astro-ph.CO].

Mesinger, A., Greig, B., & Sobacchi, E. 2016, MNRAS, 459, 2342. issn: 1365-2966. https://doi.org/10.1093/mnras/stw831.

Mitchell, D. A., Greenhill, L. J., Wayth, R. B., Sault, R. J., Lonsdale, C. J., Cappallo, R. J., Morales, M. F., & Ord, S. M. 2008, IEEE JSTSP, 2, 707. issn: 1941-0484. https://doi.org/10.1109/jstsp.2008.2005327.

Munshi, S., et al. 2025, https://doi.org/10.48550/ARXIV.2507.10533.

Munshi, S., et al. 2024, A&A, 681, A62. issn: 1432-0746. https://doi.org/10.1051/0004-6361/202348329.

Nunhokee, C. D., et al. 2025, ApJ, 989, 57. https://doi.org/10.3847/1538-4357/adda45. arXiv: 2505.09097 [astro-ph.CO].

Nunhokee, C. D., Null, D., Trott, C., Jordan, C., Line, J. L. B., BruceWayth, R., & Barry, N. 2024, PASA, 41, e095. https://doi.org/10.1017/pasa.2024.87. arXiv: 2409.03232 [astro-ph.CO].

Nunhokee, C. D., et al. 2020, ApJ, 897, 5. https://doi.org/10.3847/1538-4357/ab9634. arXiv: 2005.12174 [astro-ph.IM].

Offringa, A. R., et al. 2014, MNRAS, 444, 606. issn: 1365-2966. https://doi.org/10.1093/mnras/stu1368.

Offringa, A. R., et al. 2015, PASA, 32. issn: 1448-6083. https://doi.org/10.1017/pasa.2015.7.
Paciga, G., et al. 2011, MNRAS, 413, 1174. issn: 0035-8711. https://doi.org/10.1111/j.1365-2966.2011.18208.x.
Pritchard, J. R., & Loeb, A. 2012, RPPh, 75, 086901. issn: 1361-6633. https://doi.org/10.1088/0034-4885/75/8/086901.
Procopio, P., et al. 2017, PASA, 34. issn: 1448-6083. https://doi.org/10.1017/pasa.2017.26.
Rahimi, M., et al. 2021, MNRAS, 508, 5954. issn: 1365-2966. https://doi.org/10.1093/mnras/stab2918.
Sokolowski, M., et al. 2017, PASA, 34. issn: 1448-6083. https://doi.org/10.1017/pasa.2017.54.
Storey, J. W. V., Ashley, M. C. B., Naray, M., & Lloyd, J. P. 1994, AJPh, 62, 1077. issn: 1943-2909. https://doi.org/10.1119/1.17664.
Swarup, G., Ananthakrishnan, S., Kapahi, V. K., Rao, A. P., Subrahmanya, C. R., & Kulkarni, V. K. 1991, CSci, 60, 95. issn: 00113891, accessed March 23, 2025. http://www.jstor.org/stable/24094934.
Tingay, S. J., et al. 2013, PASA, 30. issn: 1448-6083. https://doi.org/10.1017/pasa.2012.007.
Trott, C. M., et al. 2020, MNRAS, 493, 4711. https://doi.org/10.1093/mnras/staa414. arXiv: 2002.02575 [astro-ph.CO].
Trott, C. M., Wayth, R. B., Macquart, J.-P. R., & Tingay, S. J. 2011, ApJ, 731, 81. https://doi.org/10.1088/0004-637X/731/2/81. arXiv: 1102.3746 [astro-ph.IM].
van Haarlem, M. P., et al. 2013, A&A, 556, A2. issn: 1432-0746. https://doi.org/10.1051/0004-6361/201220873.
Virtanen, P., et al. 2020, NM, 17, 261. issn: 1548-7105. https://doi.org/10.1038/s41592-019-0686-2.
Warnick, K. F., Maaskant, R., Ivashina, M. V., Davidson, D. B., & Jeffs, B. D. 2018, Phased Arrays for Radio Astronomy, Remote Sensing, and Satellite Communications (Cambridge University Press). isbn: 9781108539258. https://doi.org/10.1017/9781108539258.
Wayth, R. B., et al. 2015, PASA, 32, e025. https://doi.org/10.1017/pasa.2015.26. arXiv: 1505.06041 [astro-ph.IM].
Wayth, R. B., et al. 2018, PASA, 35, e033. https://doi.org/10.1017/pasa.2018.37. arXiv: 1809.06466 [astro-ph.IM].
Yatawatta, S., et al. 2013, A&A, 550, A136. issn: 1432-0746. https://doi.org/10.1051/0004-6361/201220874.
Yatawatta, S. 2015, MNRAS, 449, 4506. issn: 1365-2966. https://doi.org/10.1093/mnras/stv596.
Zarka, P., et al. 2015, in 2015 International Conference on Antenna Theory and Techniques (ICATT) (IEEE), 1–6. https://doi.org/10.1109/icatt.2015.7136773.
Zheng, Q., Wu, X.-P., Guo, Q., Johnston-Hollitt, M., Shan, H., Duchesne, S. W., & Li, W. 2020, MNRAS, 499, 3434. issn: 1365-2966. https://doi.org/10.1093/mnras/staa3011.

Appendix A. Image metrics

This appendix contains figures for the image RMS and dynamic range metrics for the HERA LST 5.2, SKAEOR5, and SKAEOR15 fields for comparison. A low RMS and large dynamic range are ideal behaviours for these metrics. Interestingly, the SKAEOR5 field (Figure A2) displays slowly varying RMS over a large number of observations.

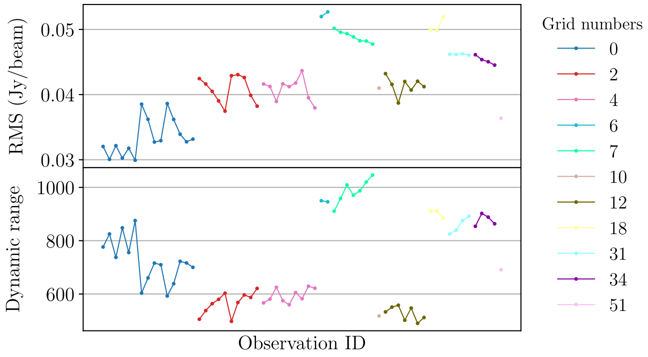

Figure A1. The RMS of the HERA field at LST 5.2 is shown in the top plot, and the dynamic range is shown in the bottom plot. Different colours correspond to different grid numbers in the field. Each point within each pointing corresponds to an observation ID, with observation IDs increasing within a pointing.

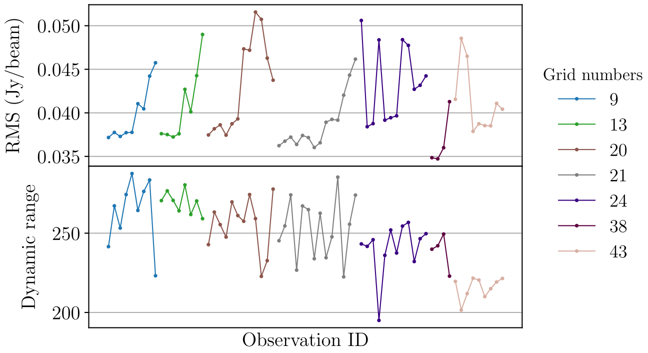

Figure A2. The RMS of the SKAEOR5 field is shown in the top plot, and the dynamic range is shown in the bottom plot. Different colours correspond to different grid numbers in the field. Each point within each pointing corresponds to an observation ID, with observation IDs increasing within a pointing.

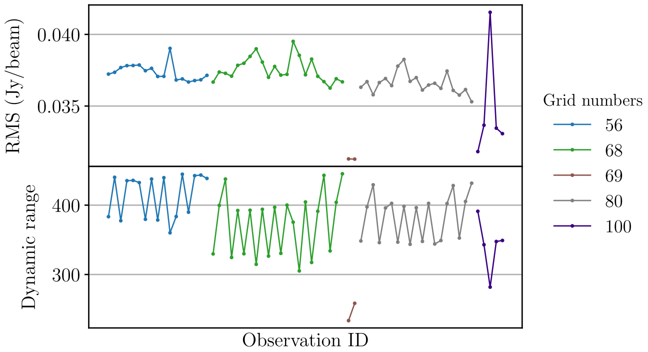

Figure A3. The RMS of the SKAEOR15 field is shown in the top plot, and the dynamic range is shown in the bottom plot. Different colours correspond to different grid numbers in the field. Each point within each pointing corresponds to an observation ID, with observation IDs increasing within a pointing.

Appendix B. Amplitude smoothness

This appendix contains figures for the calibration amplitude smoothness metric for the HERA LST 5.2, SKAEOR5, and SKAEOR15 fields for comparison. Alongside these figures, the HERA LST 2.0 field is presented to show the clustering behaviour of observations, likely arising from a lack of observations. This metric indicates smoother amplitude solutions when it is occupies values closer to 0.

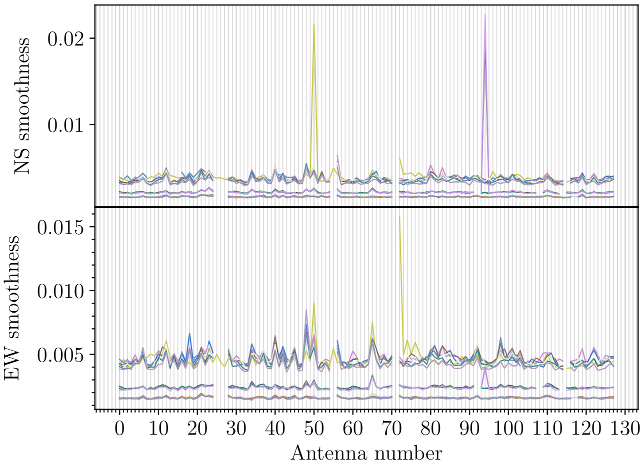

Figure B1. Smoothness of the NS (top) and EW (bottom) amplitude calibration solutions for HERA LST 2.0 for each antenna. Different colours represent a different observation ID. A lower value is ideal and indicates smoother calibration amplitude solutions. The clear grouping of observations likely arise from a lack of data for this field.

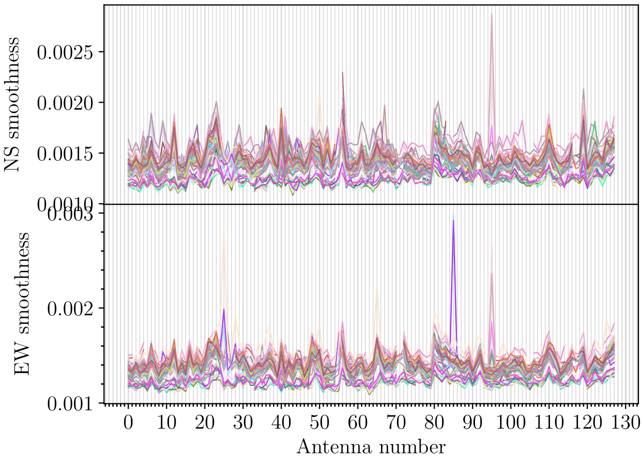

Figure B2. Smoothness of the NS (top) and EW (bottom) amplitude calibration solutions for HERA LST 5.2 for each antenna. Different colours represent a different observation ID. A lower value is ideal and indicates smoother calibration amplitude solutions

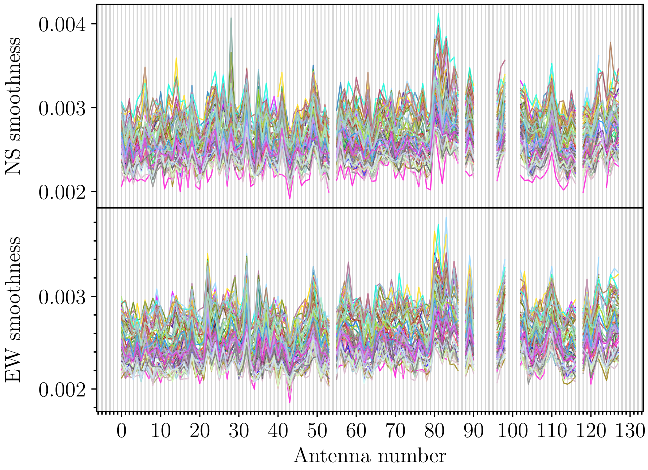

Figure B3. Smoothness of the NS (top) and EW (bottom) amplitude calibration solutions for SKAEOR5 for each antenna. Different colours represent a different observation ID. A lower value is ideal and indicates smoother calibration amplitude solutions.

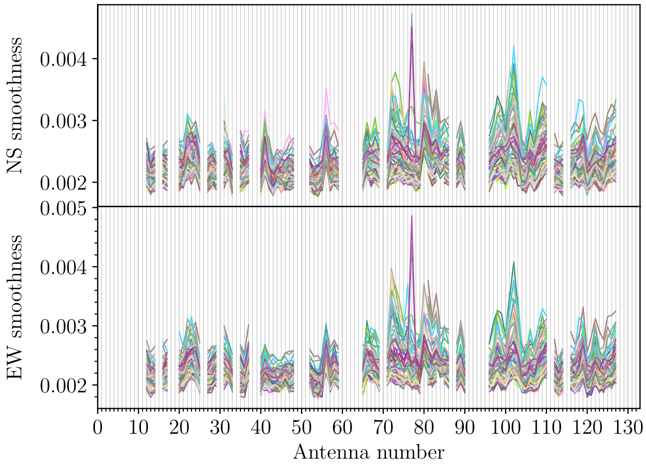

Figure B4. Smoothness of the NS (top) and EW (bottom) amplitude calibration solutions for SKAEOR15 for each antenna. Different colours represent a different observation ID. A lower value is ideal and indicates smoother calibration amplitude solutions.

Appendix C. Smoothness band plots

This appendix contains figures for the calibration amplitude smoothness metric for the HERA LST 5.2, SKAEOR5, and SKAEOR15 fields in the form of band plots for comparison. The same data used to generate the figures in Appendix B are used here. The plotted red line in these figures is the median value at each antenna. The shaded region represents the interquartile range of the data.

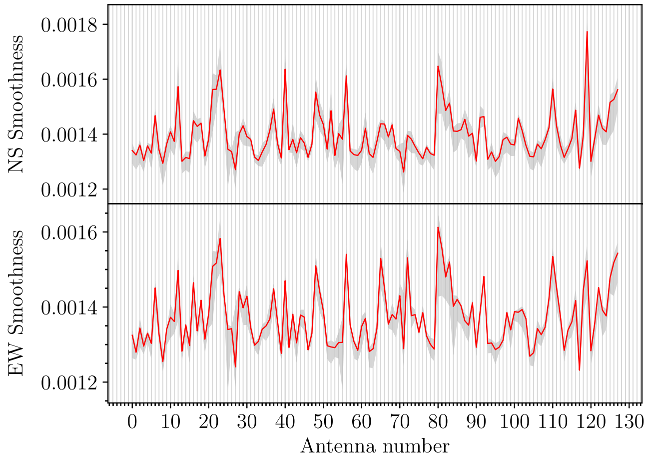

Figure C1. Smoothness of the NS (top) and EW (bottom) amplitude calibration solutions for HERA LST 5.2 for each antenna. The red line represents the median value at each antenna, while the shaded region represents the interquartile range of the data. A lower value is ideal and indicates smoother calibration amplitude solutions.

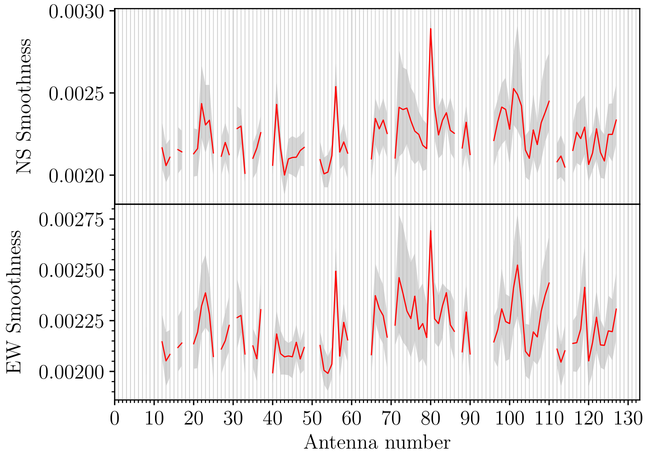

Figure C3. Smoothness of the NS (top) and EW (bottom) amplitude calibration solutions for SKAEOR15 for each antenna. The red line represents the median value at each antenna, while the shaded region represents the interquartile range of the data. A lower value is ideal and indicates smoother calibration amplitude solutions.

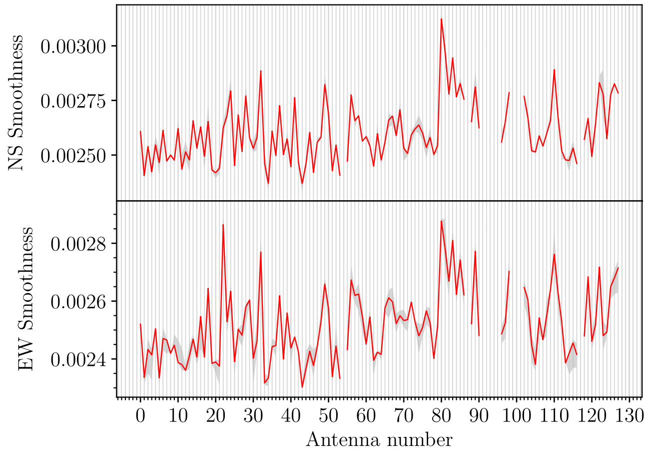

Figure C2. Smoothness of the NS (top) and EW (bottom) amplitude calibration solutions for SKAEOR5 for each antenna. The red line represents the median value at each antenna, while the shaded region represents the interquartile range of the data. A lower value is ideal and indicates smoother calibration amplitude solutions.

Appendix D. RMSE metrics

This appendix contains figures for the calibration phase RMSE metric for the HERA LST 5.2, SKAEOR5, and SKAEOR15 fields for comparison. This metric aims to measure the linearity of the phase solutions, where more linear phase solutions correspond to a lower RMSE metric.

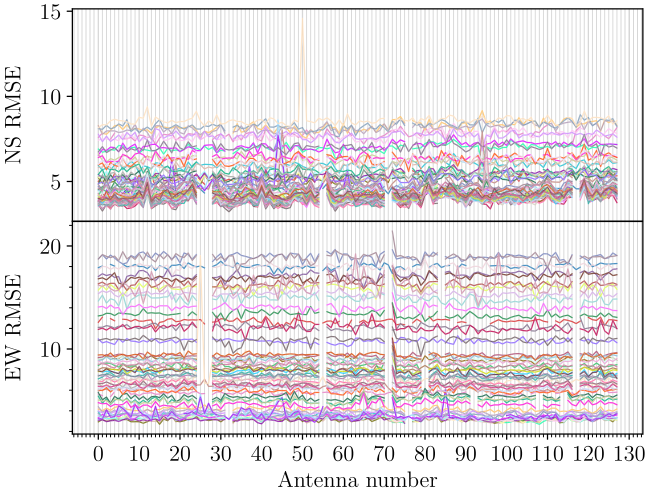

Figure D1. RMSE metric for both NS and EW cross polarisations for the HERA LST 5.2 field. Each line is a different observation. A value closer to 0 is ideal and indicates more linear phase solutions.

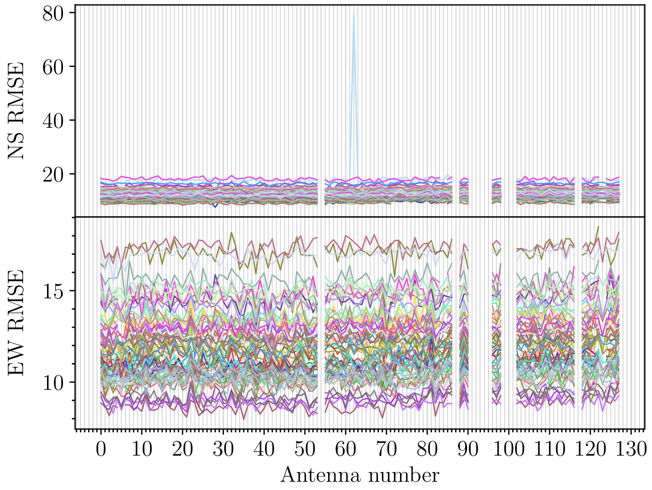

Figure D2. RMSE metric for both NS and EW cross polarisations for the SKAEOR5 field. Each line is a different observation. A value closer to 0 is ideal and indicates more linear phase solutions.

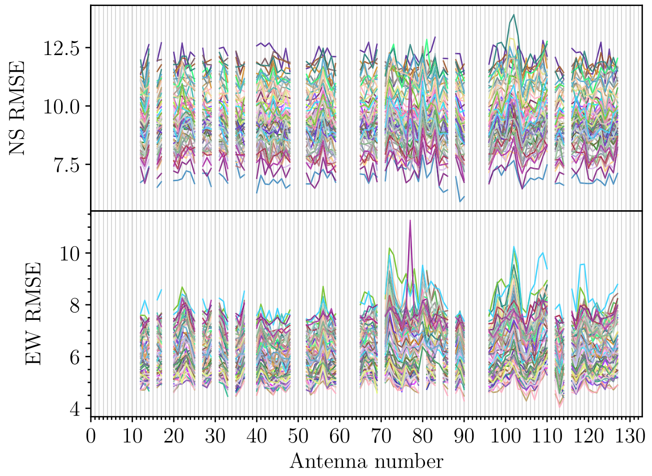

Figure D3. RMSE metric for both NS and EW cross polarisations for the SKAEOR15 field. Each line represents a different observation. A value closer to 0 is ideal and indicates more linear phase solutions.

Appendix E. Average Euclidean distance metric

This appendix contains figures for the calibration phase average Euclidean distance metric for the HERA LST 5.2, SKAEOR5, and SKAEOR15 fields.

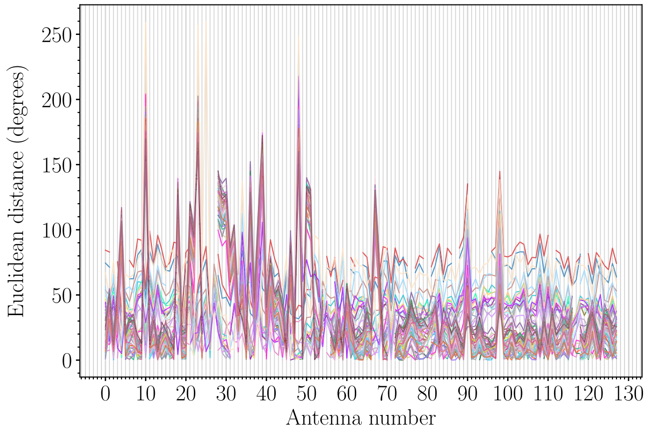

Figure E1. The average Euclidean distance between the NS and EW cross polarisations for each antenna in each observation for the HERA LST 5.2 field. A value closer to 0 is ideal and signals that the solutions are more similar.

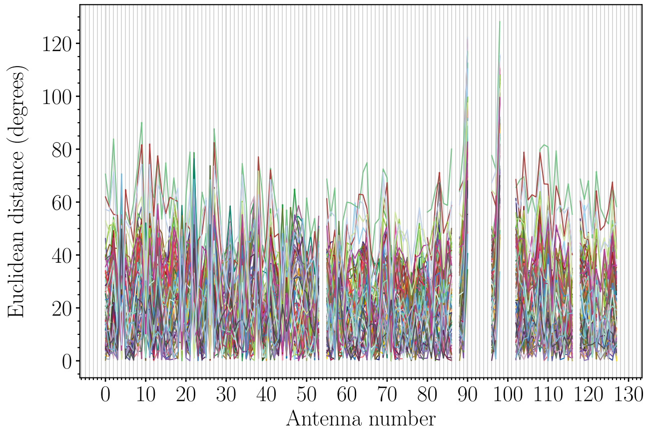

Figure E2. The Euclidean distance between the NS and EW cross polarisations for each antenna in each observation for the SKAEOR5 field. A value closer to 0 is ideal and signals that the solutions are more similar.

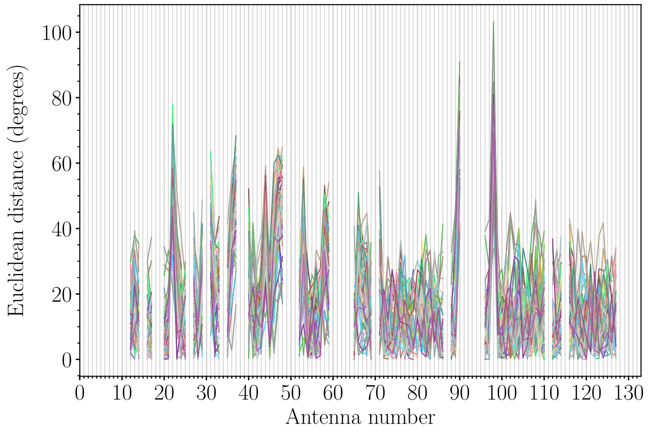

Figure E3. The Euclidean distance between the NS and EW cross polarisations for each antenna in each observation for the SKAEOR15 field. A value closer to 0 is ideal and signals that the solutions are more similar.